Nanocrystalline nickel-graphene nanoplatelets composite: Superior mechanical properties and mechanics of properties enhancement at the atomistic level

Fatemeh Yazdandoost, Ayoub Yari Boroujeni, and Reza Mirzaeifar*
Department of Mechanical Engineering, Virginia Tech, Blacksburg, Virginia 24061, USA
(Received 7 July 2017; revised manuscript received 25 September 2017; published 8 December 2017)

A relatively easy-to-fabricate nanolayered metal composite with superior mechanical properties is introduced. The matrix is a nanocrystalline nickel in which the grain size is engineered to optimize the strength, and monolayer particles of graphene are embedded into the matrix as reinforcing interlayers. Atomistic-scale deformation mechanisms, and mechanics of hindering the dislocations propagation by graphene nanoplatelets with different configurations in the nanocrystalline metallic matrix, are investigated by molecular dynamics simulations. Molecular dynamics findings are utilized to engineer the nanostructure of a metal matrix composite. Nanocrystalline nickel-graphene nanolayered systems with optimum mechanical properties are identified and fabricated with a cost-efficient method. The nanostructure of the fabricated composites is examined via electron microscopy, and their mechanical performance is inspected via nanoindentation tests. The experimental results show that a nickel-graphene nanolayered system with 14% areal coverage of graphene particles at the interlayers has improved the hardness of the nanocrystalline nickel by almost 40%.

DOI: 10.1103/PhysRevMaterials.1.076001

I. INTRODUCTION

Carbon based nanomaterials, such as carbon nanotubes (CNTs) and graphene, possess outstanding mechanical strength and stiffness, as well as extraordinary electrical and thermal conductivity [1–5]. Due to these excellent characteristics, they have recently drawn researchers' extensive attention for their potential application in designing and fabricating new generations of composite materials with superior mechanical and multifunctional performance. Particularly, CNTs have been widely used as reinforcing materials in various metal matrix composites (MMCs) [6–13]. Although there are reports on reduction in mechanical performance of MMCs [6] due to insufficient CNT dispersion using simple mechanical mixing approaches, improvements in the mechanical properties of the MMCs have been achieved via utilizing more complicated fabrication methods such as molecular level mixing [7,8], electrochemical codeposition [11], and CNT functionalization associated with hydrophilic metal flake coatings [13]. Strengthening effects of well-dispersed CNTs into the MMCs can be attributed to the outstanding load-bearing capability of the CNTs and their stress transfer proficiency due to the extensive filler-matrix interface area provided by the high aspect ratio of CNTs. Like CNTs, graphene nanoplatelets or nanosheets (GNSs) have been used to fabricate MMCs based on aluminum [12,14–16], copper [17–20], magnesium [21], and nickel [22]. Compared to the CNTs and due to their two-dimensional (2D) geometry, GNSs are more difficult to disperse into the metal matrices. Therefore, utilizing mechanical alloying techniques to incorporate GNSs into MMCs resulted in either deterioration [12,16] or moderate improvements [15,17] in the mechanical performance of the MMCs. However, through more complicated fabrication techniques, such as using hydrophilic metal flake coatings [14], electro codeposition [22], molecular level mixing [18], pulse reversed electrodeposition [19], hybridizing GNSs with metal nanoparticles [20], and liquid state dispersion into metal melt associated with solid-state friction stirring [21], higher volume fractions of GNSs could be dispersed into the metal matrices, resulting in better improvements in the mechanical properties.

In addition to their great mechanical properties, the unique 2D geometry of GNSs has encouraged their application in a new type of MMCs, metal nanolayered composites [23]. Metal nanolayered composites with high-density interlayers have been shown to be capable of interlocking dislocations resulting in various exceptional properties, such as ultrahigh strength and self-healing [23–26]. It is shown that the presence of single layer graphene in between single-crystal metal nanolayers could result in ultrahigh strength metal nanopillars [23]. In recent years, atomistic simulations of metal single crystals in interaction with graphene nanosheets have been used to reveal the mechanisms behind strengthening effects of GNSs on single-crystal metal nanolayered composites [23,27,28]. However, to the best of our knowledge, there are no atomistic simulations so far reporting the effect of graphene sheets in polycrystalline metals.

In the present paper, we introduce a new nickel-graphene nanolayered composite system in which, instead of using large individual graphene sheets that cover all the interlayer area, monolayer graphene flakes are spread inside the interlayers so that only a fraction of the interlayer area (13–30%) is covered. Compared to the previous similar composite systems [23], the introduced graphene-metal nanolayered composite is easier and more cost effective to fabricate in large scales. In the first steps of this paper, a systematic investigation of the effect of various graphene reinforcement configurations on a nickel-graphene system's performance is performed by utilizing a series of atomistic simulations. Molecular-dynamics (MD) simulations of various nanocrystalline nickel-graphene systems are performed, under both compression and nanoindentation loadings, to reveal the effect of graphene nanosheets

*Corresponding author: rmirzaei@vt.edu; http://www.me.vt.edu/multismart/

 ©2017 American Physical Society

on hindering the dislocation propagation inside the metallic systems. As the results, the best applicable nickel-graphene nanolayered systems are identified, fabricated, and examined in the experiments.

In order to fabricate the composites, the electron-beam evaporation technique is utilized for depositing the metal layers. As a result, a nanocrystalline structure for the nickel layers is obtained. It is well established that in polycrystalline metals there is a so-called Hall-Petch relation [29,30] between the strength and the average grain size in which the strength increases as the grain size decreases. However, it is also observed that in nanocrystalline metals with few-nanometer average grain sizes as the grain size decreases the material experiences softening, showing a reverse Hall-Petch effect [31–34]. Hence, there is an average grain size range in which a nanocrystalline metal has the maximum possible strength [35,36]. In the composite systems introduced in this paper, the nickel layers possess a nanocrystalline structure with an average grain size very close to this optimum size. Therefore, this material system benefits from both the nanocrystallinity of the metal as well as the strengthening effects of the graphene interlayers at the same time.

During the composite fabrication process, field emission scanning electron microscopy (FE-SEM) associated with an image processing tool is employed to investigate the quality of the graphene flake dispersion over the interlayer areas. Furthermore, the crystalline structure of the nickel layers is examined via SEM and transmission electron microscopy (TEM). The fabricated nickel-graphene nanolayered composites are mechanically characterized with nanoindentation experiments to quantify their hardness to confirm the extraordinary strengthening effects of graphene particles on nanocrystalline nickel nanolayered composites.

II. MATERIALS AND METHODS

A. Computational modeling

A series of MD simulations are performed to investigate the effects of various designs on the mechanical performance of nickel-graphene composites. An accurate modified embedded atom method (MEAM) potential for nickel-graphene, developed by Uddin *et al.* [37], is used in this paper. In the MEAM potential, the total energy of the system is given as

$$E = \sum_i \left[F_i(\bar{\rho}_i) + \frac{1}{2} \sum_{j(\neq i)} S_{ij} \varphi_{ij}(R_{ij}) \right], \tag{1}$$

where F_i, S_{ij}, and $\varphi_{ij}(R_{ij})$ are the embedding function for an atom i and the screening function and pair interaction between atoms i and j which are separated by a distance R_{ij}, respectively. Parameter $\bar{\rho}_i$ is the electron background density. The electron background density at each site is computed by combining several partial electron-density terms for various angular contributions with weight factors $t^{(h)}(h = 0 - 3)$. Each partial electron density is a function of atomic configuration and atomic electron density. The atomic electron densities $\rho^{\alpha(h)}(h = 0 - 3)$ are given in the form

$$\rho^{\alpha(h)}(R) = \rho_0 \exp\left[-\beta^{(h)} \left(\frac{R}{r_c} - 1 \right) \right], \tag{2}$$

where ρ_0 and $\beta^{(h)}$ are the atomic electron-density scaling factor and the decay length, respectively, and both are adjustable parameters. r_c is the nearest-neighbor distance in the equilibrium reference structure. The coefficients of this potential for the nickel-graphene system are calculated and reported by Uddin *et al.* [37].

All the molecular-dynamics simulations in this paper are performed at the finite temperature $T = 300$ K using time integration on Nose-Hoover style non-Hamiltonian equations of motion in isothermal-isobaric ensembles. The large-scale atomic/molecular massively parallel simulator (LAMMPS) [38] is utilized for performing the simulations, and the Ovito [39] visualization tool is used for postprocessing the results of MD simulations. Two three-dimensional (3D) periodic cells of nickel are created in two different sizes, $500 \times 500 \times 500$ and $250 \times 250 \times 250$ Å. For each periodic cell, two types of polycrystals, possessing 10 and 100 grains, are created using the Voronoi Tessellation algorithm [40]. As a result, two polycrystalline samples with average grain sizes of 24.8 and 11.9 nm are obtained from the bigger cell size, and two polycrystalline samples with average grain sizes of 12.4 and 5.9 nm are modeled using the smaller cell size.

The MD simulations are performed for four different embedded graphene configurations: (a) no graphene, (b) layerwise-arranged graphene particles, (c) layerwise-arranged graphene full sheets representing continuous large sheets of graphene in the matrix, and finally (d) randomly oriented graphene particles in the grains. The graphene inserts are first embedded into the polycrystals and then the overlapped nickel atoms are deleted. This method of incorporating the graphene particles into a polycrystalline metal will put the graphene inserts inside the nickel grains, not necessarily in the grain boundaries. This assumption of graphene arrangements inside the metal grains is not far from reality, since the exceptionally low thickness of monolayer graphene would allow continuation of epitaxial [41] metal crystal growth [21,23].

The systems are equilibrated at $T = 300$ K for 20 ps. After equilibrium, the simulation boxes are deformed in compression to about 10% of their original size in the z direction, which is perpendicular to the graphene planes, during 100- and 50-ps loading times. These two loading conditions represent the strain rates of 10^9 and 2×10^9 s^{-1}. For simulating the materials performance under indentation loadings, a 3D computational cell of nickel-graphene with the size of $250 \times 250 \times 250$ Å with ten grains is modeled and a spherical indenter with the radius of 50 Å is utilized to indent the system. The system is periodic in x and y directions. After equilibration at $T = 300$ K for 20 ps, the system is compressed by the indenter in the z direction for 100 ps and then unloaded for 100 ps while the two bottom atomic layers are fixed. More details of implementing MD to study metallic systems, and particularly tracking the structural changes in the crystal structure, are reported in our recent works [42–44].

Note that the compression loading along the z direction (perpendicular to the graphene nanosheets) was chosen for the main MD simulations in favor of consistency between the numerical and experimental studies (as discussed in Sec. II C). However, since the material system introduced in this paper is anisotropic, several MD simulations with both the tensile and compressive loadings along the three different directions

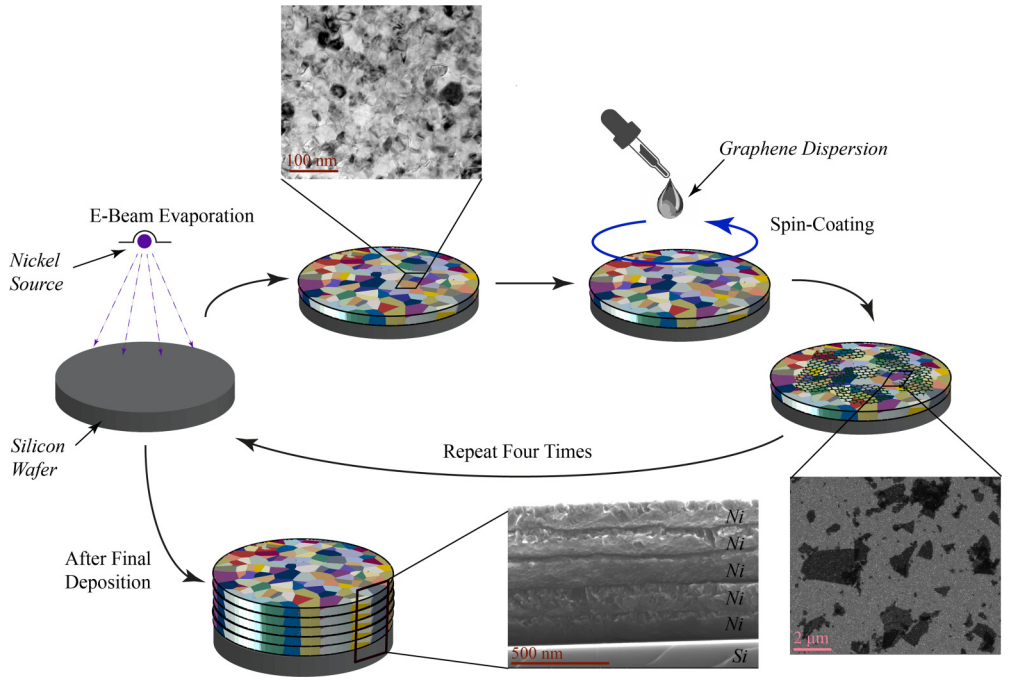

FIG. 1. Schematic sketch of the nickel-graphene nanolayered composites fabrication. E-beam evaporation is used to deposit the first nickel layer on the silicon substrate. Graphene particles dispersion in water is spin coated over the nickel layers. The whole process is repeated four times to achieve five-layered nickel-graphene composite nanolaminates. Scanning electron microscopy is used to investigate the quality of the graphene particles spread over nickel layers, as well as the cross section of the fabricated composites. Transmission electron microscopy is used to evaluate the crystallinity of the nickel layers.

are performed to clarify the contribution of graphene particles in strengthening the designed nickel nanolayered composites under various modes of deformation. MD simulations results are reported and discussed in Sec. III A as well as in the Supplemental Material [45].

B. Composites fabrication and characterization

Figure 1 summarizes the steps towards fabricating the nickel-graphene nanolayered composites and how electron microscopy is employed to characterize the fabricated composites. As shown in the figure, circular wafers of Si ⟨100⟩ single crystal with diameters of 25.4 mm, by UniversityWafer, Inc., are used as substrates for fabricating the nickel-graphene nanolayered composites. A PVD-250 E-beam evaporation system, by Kurt J. Lesker, Co., is employed for metal thin-film depositions. As the first layer, a 20-nm-thick film of titanium is deposited over the clean silicon wafers in order to improve the adhesion between the material and the substrates. Then, a 150-nm-thick layer of nickel is deposited over the titanium coated silicon wafers at 2.0-Å/s deposition rate under 5.0×10^{-6}-Torr pressure. The deposition rate is monitored *in situ* by a crystal thickness monitor mounted inside the PVD-250 chamber. After nickel deposition, the silicon wafers are taken out of the E-beam evaporation chamber in order to start the graphene layer insertion procedure.

The graphene layer insertion procedure is performed via spin coating of aquatic dispersions of graphene flakes over nickel coated wafers. The aquatic solutions contained four different concentrations of graphene flakes: 0.025-, 0.050-, 0.075-, and 0.100-wt. % graphene in water. The desired concentrations are obtained from adding deionized (DI) water in a 1.0-wt. % research grade graphene water dispersion, by US Research Nanomaterials, Inc. According to the specifications by the vendor, the graphene nanoplatelets possessed 0.55–1.2-nm thickness, which corresponds to monolayer and double layer graphene, and 1–12-μm diameter. The graphene dimensions are confirmed later with electron microscopy. The spin-coating procedure is performed at 2000-rpm speed for 40 s. As a result of spin coating the various graphene concentrations' various coating configurations of graphene flakes over the nickel metal deposited samples are obtained.

After this procedure, the graphene coated samples are put back in the E-beam evaporation chamber to deposit another layer of 150-nm-thick nickel over the samples. The graphene and nickel deposition cycles are repeated three times more in order to obtain the designed nickel-graphene nanolayered composites. At the end of the sample preparation procedure, the samples possess five layers of 150-nm-thick nickel metal. Between each two neighboring nickel layers, a thin layer of graphene particles is embedded. The samples are labeled as R (reference), D (dilute), M (medium), H (high), and SH (superhigh), representing the corresponding contained graphene dispersion concentrations. In other words, the samples named D, M, H, and SH undergo the spin coatings of graphene dispersion concentrations of 0.025, 0.050, 0.075, and 0.100 wt. %, respectively, and the R sample does not have any graphene layer.

A LEO (Zeiss) 1550 field-emission scanning electron microscope is used to examine the quality of the graphene coatings over the nickel layers. The same FE-SEM system is

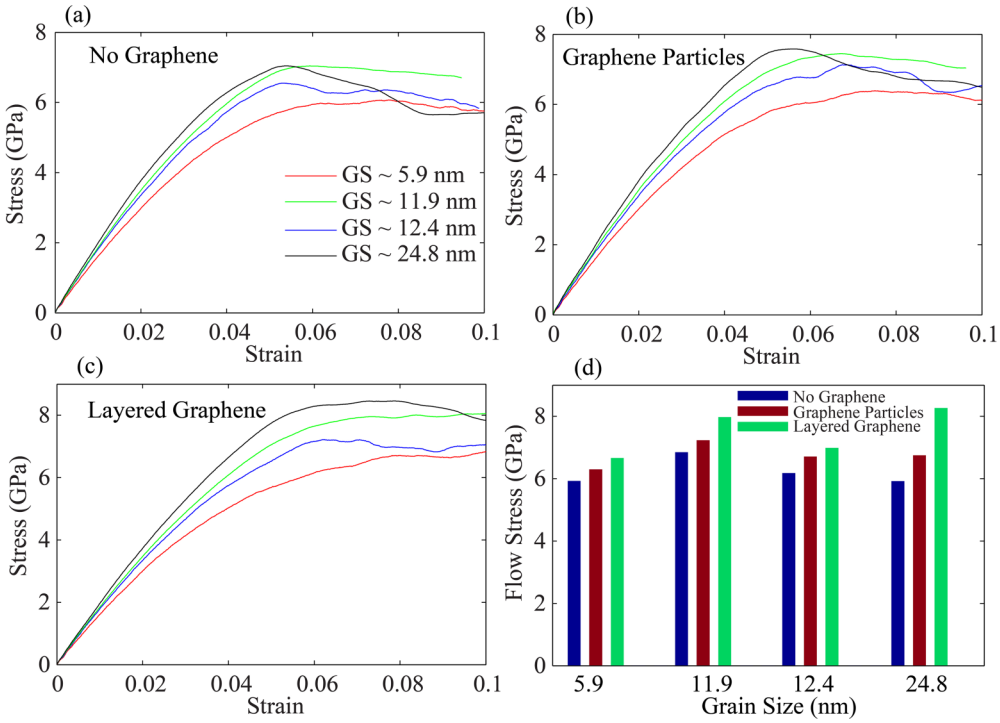

FIG. 2. Compressive stress-strain response of the nanocrystalline nickel layered systems with different average grain sizes (GS) under compression loading at the strain rate of $10^9\ s^{-1}$ for the systems with (a) no graphene, (b) graphene particles, and (c) layered graphene full sheets. (d) Flow stress obtained from the stress-strain curves at different average grain sizes of the nanocrystals. It is evident that the pure nanocrystalline nickels with the average grain size of ~12 nm possess the optimum grain size to have the highest flow stress under compressive loads. Both the graphene particles and graphene full sheet interlayers have strengthening effects on the nanocrystalline nickels with different average grain sizes.

used to see the cross section of the nanolayered composites to confirm the uniformity of the nickel layers and probe their crystallinity. The coated silicon wafers are freeze fractured using liquid nitrogen in order to prepare their cross section for the electron microscopy. TEM samples are also prepared and a JOEL 2100 transmission electron microscope is employed to study the crystalline structure of the nickel layers. Selected area diffraction patterns (SADPs) are obtained to confirm and quantify the crystallinity of the nanolayered nickel samples.

C. Nanoindentations

A NanoTest, by Micromaterials, Inc., is used to perform nanoindentation tests on the fabricated nickel-graphene nanolayered composites in order to study the effect of different graphene particles at the interlayers on the elastic modulus and hardness of the composites. The load-controlled nanoindentation tests are performed using a diamond Berkovich indenter tip at three maximum load levels of 5.0, 10.0, and 20.0 mN. Nine indentations are done per load case under fixed 20-s loading, 5.0-s dwell period at maximum load, and 20-s unloading times. The load-depth data are recorded during the nanoindentation tests and the data are corrected for thermal drift using a 30-s dwell period at 10% maximum load. The data are analyzed using the Oliver-Pharr method [46,47] to obtain the hardness and reduced modulus of the nickel-graphene composites.

III. RESULTS AND DISCUSSION

A. Computational results

1. *Strengthening mechanisms and grain size effect*

Compressive stress-strain curves, for the atomistic simulation models under compressive loadings at 10^9-s^{-1} strain rate, are shown in Fig. 2 for four different average grain sizes. Figure 2(a) shows the compressive stress-strain behavior when there is no graphene inside the polycrystalline nickel grains, while Figs. 2(b) and 2(c) represent the results when graphene particles and graphene full sheets are added, respectively, as layers into the nanocrystalline nickel structures. Strength is indicated by flow stress values shown in Fig. 2(d). The flow stress is calculated as the average of the stress values obtained from the stress-strain curves beyond the strain level of 0.07 after which the stress-strain curves for almost all the material systems exhibit a plateaulike behavior. Comparing the results of nickel nanocrystals with no graphene, it can be seen that as the average grain size decreases from 24.8 to 11.9 nm the flow stress increases, and as the grain size decreases further to 5.9 nm the flow stress drops. These results are in agreement with the reported values in the literature [31–34]. This phenomenon is due to different deformation mechanisms in nanocrystalline metals, where at coarser grain sizes (>12 nm) plastic deformation is mostly governed by dislocation nucleation and growth through the grains, representing the so-called Hall-Petch effect, while at finer grain sizes (<12 nm) the role

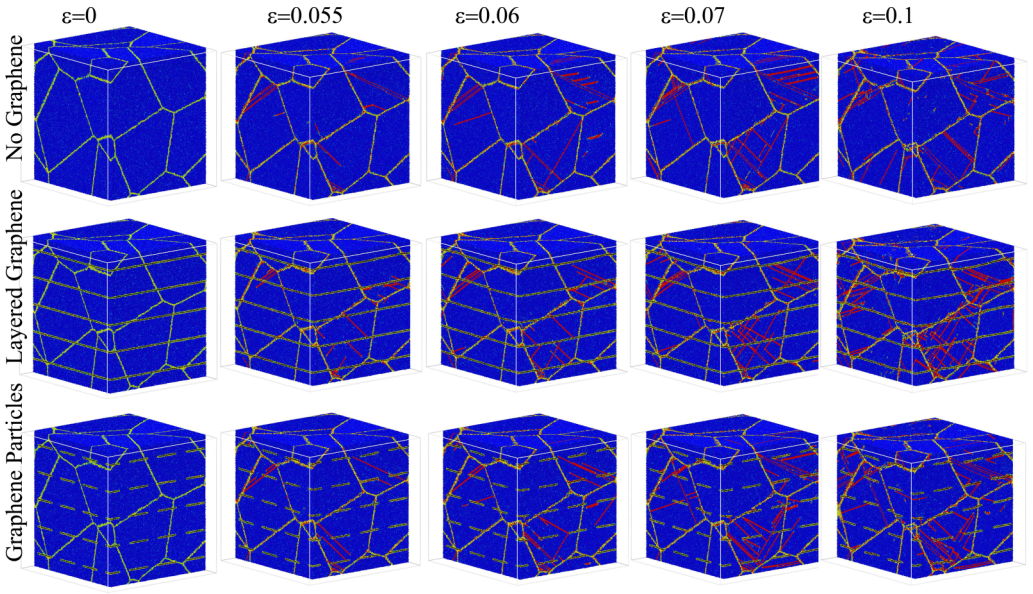

FIG. 3. Deformation steps of nanocrystalline nickels with average grain size of 24.8 nm reinforced with no-graphene (first row), layered graphene sheets (second row), and graphene particles (third row) interlayers under compression strain loading up to 0.10. The dislocations travel through the grain as the strain increases unless they are stopped by grain boundaries (in the first row), layered graphene (second row), and graphene particles (third row).

of the atomic sliding at the grain boundaries in the plastic deformation gets more highlighted, illustrating a reverse Hall-Petch effect. Since the simulations start at a dislocation-free situation, for coarse-grained nanocrystal systems, high stress is needed to nucleate dislocations inside the grains. However, as dislocations start to move inside the grains, due to the large grain sizes, significant plastic deformation occurs and stress is released to some extent. That is the reason for the compressive stress-strain curves of the coarse-grained models to demonstrate an overshot peak [35].

It is well established in the literature that nanocrystalline metals reach a maximum strength at an average grain size in which the Hall-Petch deformation regime transfers to the reverse Hall-Petch regime [35]. For nickel nanocrystals, this crossover, which is corresponding to the maximum possible strength, occurs around 10–12-nm average grain size [36], which is evident from the results of Fig. 2. However, when graphene layers are added into the nickel nanocrystalline structure, the strength of the nanocrystals improves even further. This improvement in the strength is achieved at all the grain sizes reinforced with both the layered graphene full sheets and the nickel particles interlayers.

Inferred from the results of Fig. 2(d), the improvement in flow stress via adding the layered graphene sheets is more pronounced in the coarse-grained structures where ∼40% improvement was obtained. The mechanism behind this significant improvement can be observed in Fig. 3. As shown in the top row in Fig. 3, as the applied strain goes beyond 0.055, the nucleated dislocations tend to grow through the grains up to the point that they are hindered by the grain boundaries. However, in the presence of graphene interlayers (second row of Fig. 3), the growing dislocation loops are almost fully trapped by graphene sheets at earlier stages of their propagation. This mechanism limits the plastic deformation, explaining the significant strengthening effect of layered graphene sheets. A similar trend is observed in the nickel nanocrystals reinforced with layers of graphene particles (third row of Fig. 3).

Taking a closer look at a cross-sectional cut from the graphene reinforced nanocrystals, provided in Fig. 4, reveals the interaction between graphene layers and dislocation motions. As shown in Figs. 4(a) and 4(c), the dislocations, grown inside the grains above and below the graphene layer, are fully stopped when they meet graphene. However, in the presence of graphene particles, shown in Figs. 4(b) and 4(d), some dislocations are fully, and some are partially, hindered by the graphene flakes. These dislocation motion stoppage mechanisms have caused the compressive stress-strain response of the nanocrystal systems to delay the onset of yielding [Fig. 4(d)], resulting in exhibiting higher flow stress. Therefore, as quantitatively shown in Fig. 2(d), 14 and 40% improvements in the strength of the nickel nanocrystal with an average grain size of 24.8 nm were obtained via reinforcing with layered graphene sheets and graphene particles, respectively.

In case of nanocrystals with finer average grain sizes (e.g., 11.9 nm) similar strengthening effects can be observed when the reinforcing graphene interlayers are added into the systems. Figure 5 shows these nanocrystals under compressive loading, revealing how the deformation mechanisms set as compressive strain increases.

In the case of nanocrystalline nickels with the average grain size of 11.9 nm, the governing plastic deformation mechanism is a mixture of Hall-Petch and reverse Hall-Petch effects. Hence, compared to the coarse-grained systems shown in Figs. 3 and 4, the reinforcing graphenes, embedded into the fine-grained systems of Fig. 5, act slightly differently in strengthening the system. Figure 6 shows a magnified view of cross-sectional cuts from the graphene reinforced nickel nanocrystalline systems under high compressive strain.

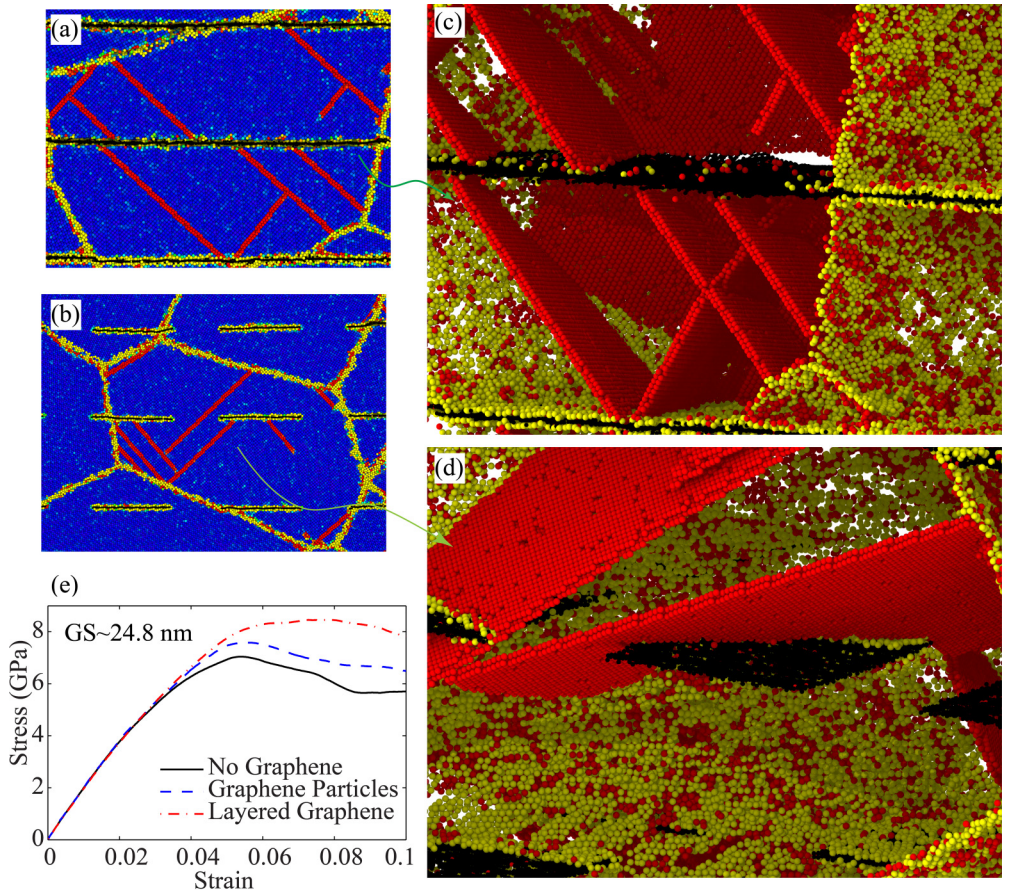

FIG. 4. Strengthening mechanism in the nanocrystalline nickels with average grain size of 24.8 nm reinforced with (a and c) layered graphene sheets and (b and d) graphene particles. It is shown how dislocations motions are fully stopped by graphene sheets and partially stopped by graphene particles. (e) Comparative compressive stress-strain curves of the systems reinforced differently. It is evident that graphene interlayers have raised the flow stress.

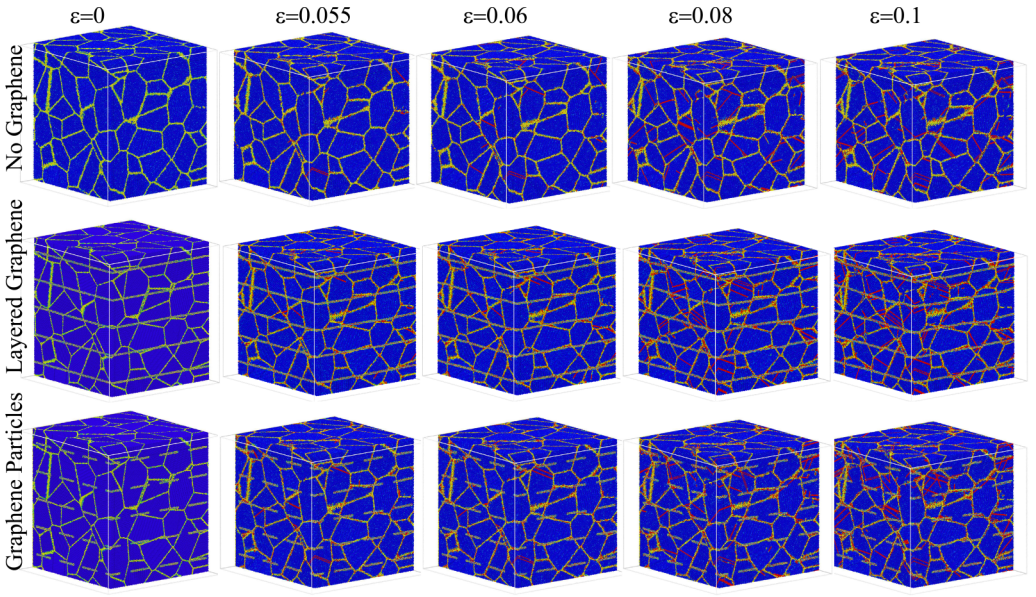

FIG. 5. Deformation steps of nanocrystalline nickels with average grain size of 11.9 nm reinforced with no-graphene (first row), layered graphene sheets (second row), and graphene particles (third row) interlayers under compression strain loading up to 0.10. The dislocations travel through the grain as the strain increases unless they are stopped by grain boundaries (in the first row), layered graphene (second row), and graphene particles (third row).

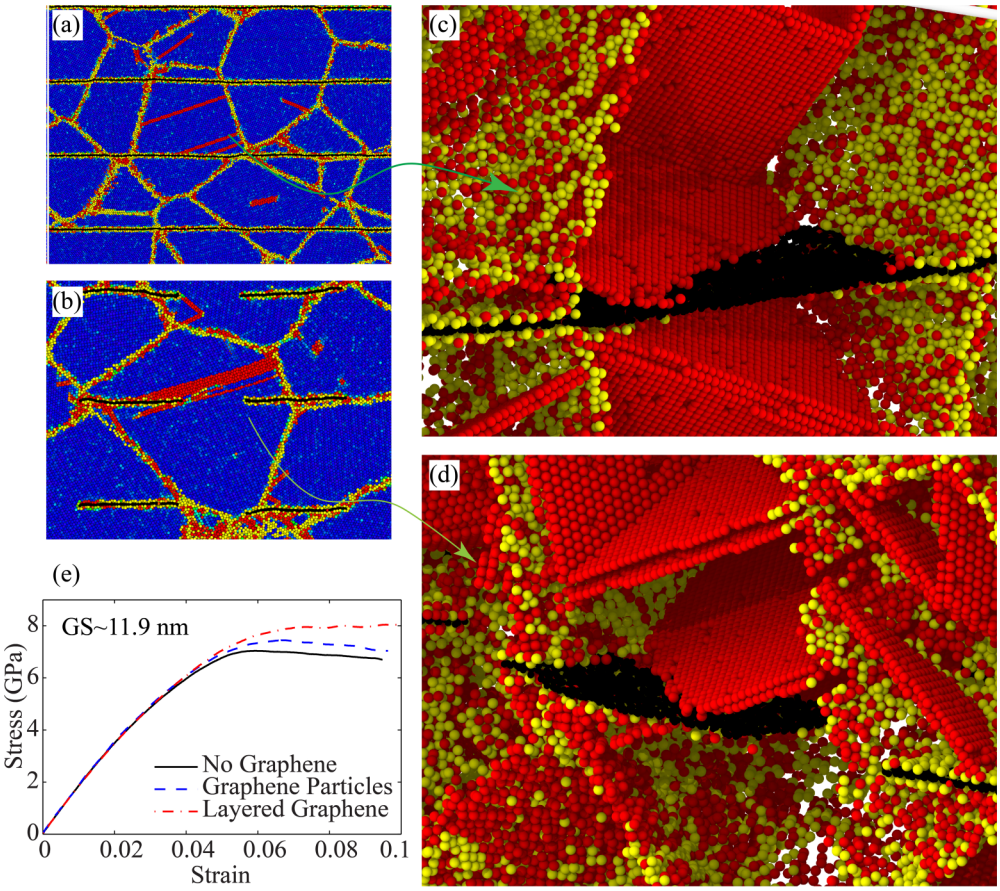

FIG. 6. Strengthening mechanism in the nickel nanocrystals with average grain size of 11.9 nm reinforced with (a and c) layered graphene sheets and (b and d) graphene particles. It is shown how dislocations motions are fully stopped by graphene sheets and partially stopped by graphene particles. Additionally, dislocation buildups at the grain boundaries due to atomic sliding are stopped by the graphene inserts. (e) Comparative compressive stress-strain curves of the systems reinforced differently showing graphene interlayers successfully increase the flow stress of the nanocrystalline nickel.

Similar to the systems with coarser grain size, growing dislocations are trapped by graphene sheets and particles. Furthermore, since atomic sliding at the grain boundaries is another plastic deformation mechanism at nanocrystals of this grain size, it can be seen that dislocation buildups due to atomic sliding at grain boundaries are stopped by graphene layers. Particularly, in Fig. 6(b) graphene particles are deformed slightly to prevent the atoms at the grain boundaries from sliding. Comparing the systems with the graphene particles and layered graphene sheets, the latter system has a greater chance to contribute to the strengthening mechanism. Therefore, in the compressive stress-strain curves illustrated in Fig. 6(e), the system with the layered graphene exhibits higher flow stress than the system with graphene particles. However, the graphene particles were also successful to fully or partially block the dislocation growth.

2. *Strengthening effects of graphene particles under other modes of deformation*

As mentioned in Sec. II A, two more series of MD simulations are performed on the material systems with the average grain size of 12.4 nm, which in the first one, the tensile strain, and in the second one, compressive strain, is applied along the three principal directions. The tensile and compressive stress-strain curves are shown, respectively, in Figs. S1 and S2 of the Supplemental Material [45] for the models with and without layered graphene particle reinforcements. The tensile and compressive flow stress values for each stress-strain curve are calculated and presented in the bar chart of Fig. S3 [45]. For all the loading modes and directions, the nanocrystalline nickel shows improvements in the flow stress due to existence of graphene particle interlayers. This strength improvement can be attributed to the dislocation blocking capabilities of the graphene particles explained in Sec. III A 1.

Figure S4 illustrates a comparison between the stress-strain response of the material systems in tension and compression [45]. For both the systems with and without graphene reinforcements, the compressive strength is higher than tensile strength. This tension compression asymmetry has been reported in the literature for nanocrystalline metals [48,49]. This is due to the fact that in the nanocrystalline metals dislocations emission occurs with more difficulty under the existence of compressive stress than under tensile stress [48,49]. However, the existence of the interlayer graphene nanosheets has increased the strength both in tension and compression.

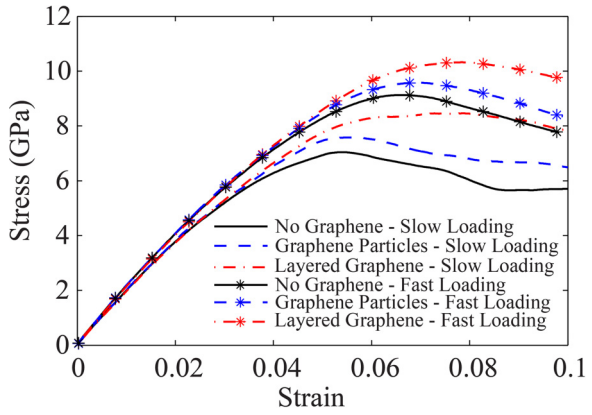

FIG. 7. Compressive stress-strain behavior of the nickel crystalline systems reinforced with no graphene, graphene particles, and layered graphene sheets under slow loadings at the strain rate of 10^9 s^{-1} and faster loading at the strain rate of 2×10^9 s^{-1}. The curves for the higher strain rate loading illustrate overshoots. However, these overshoots are followed by drops in stress level. Regardless of strain rate, the graphene interlayers successfully increase the flow stress at nanocrystalline nickel composites.

3. *Loading rate effect*

In addition to the aforementioned atomistic simulations performed at 10^9-s^{-1} strain rate, a series of simulations are also performed at 2×10^9-s^{-1} strain rate, in order to study the effect of loading rate on the strengthening mechanisms of graphene interlayers. Figure 7 shows the compressive stress-strain curves for the system with average grain size of 24.8 nm with different configurations of graphene interlayers at the two above-mentioned strain rates. As well established in the literature [35], when the strain rate increases, higher stress is needed to be built up to nucleate dislocations from the grain boundary sources, and, as strain increases further, significant plastic deformations and therefore a drop in the stress level appear due to growing the dislocation inside the grains. This phenomenon is more evident in coarser-grained polycrystals. Therefore, a jump in the stress-strain curves associated with a distinctive peak can be seen for the systems with no graphene interlayers. However, at the lower strain rate, the existence of graphene interlayers, especially the layered graphene sheets, stops the nucleated dislocations from growing, resulting in maintaining the stress level. Hence, the reinforcing capabilities

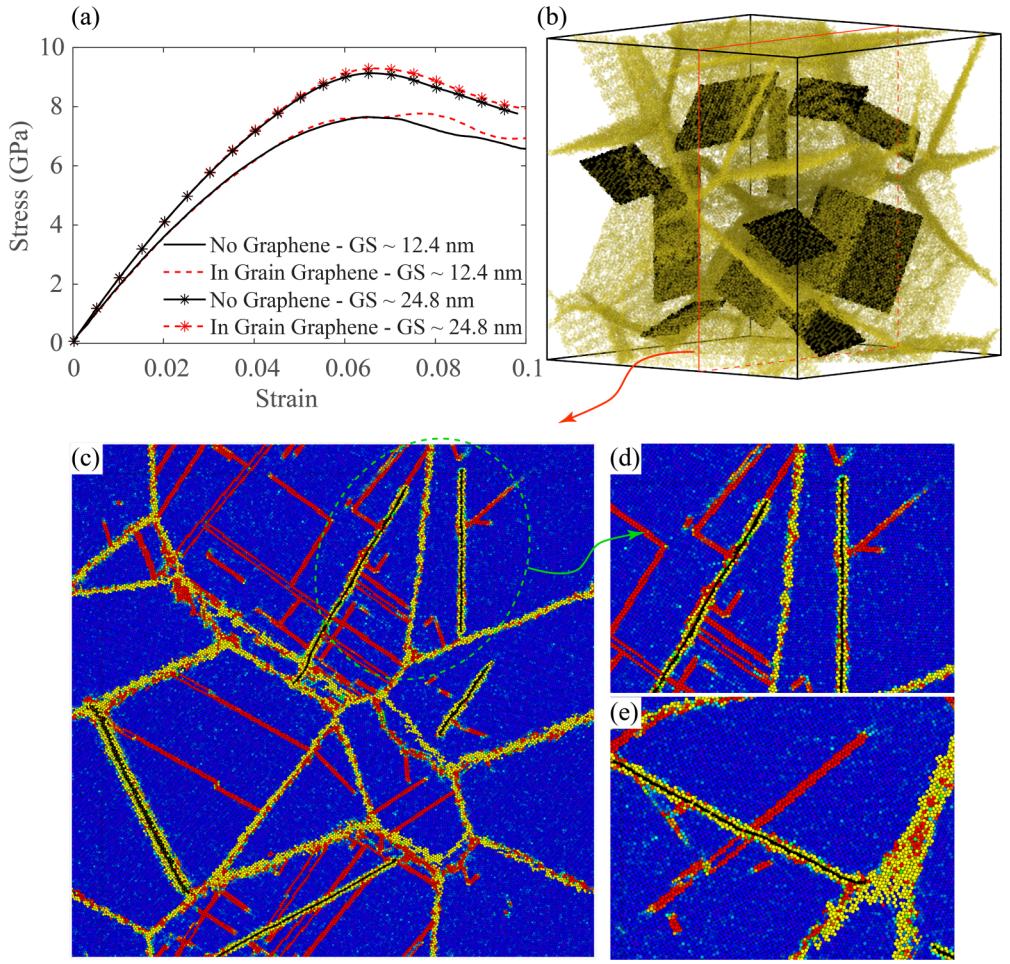

FIG. 8. Performance of the nanocrystalline nickel samples with two different average grain sizes reinforced with randomly oriented graphene particles under fast loading rate. (a) Compressive stress-strain response. (b) Graphene arrangement inside a nickel nanocrystal. (c) Cross-sectional cut showing interactions of graphene and dislocations. (d) Graphene particles with dislocations initiated at their tip. (e) A graphene particle that has stopped dislocations motion. Inferred from the stress-strain curves, the deteriorating and strengthening effects of randomly oriented graphene particles cancel out each other.

of the graphene interlayers are more significant at lower strain rates.

4. Random orientation of graphene dispersion

As discussed in the previous sections, when the graphene sheets or particles are distributed layerwise and perpendicular to the loading direction inside a nickel nanocrystalline system, significant improvements in the strength of the nickel nanocrystals can be achieved. A series of simulations is also performed to examine the effect of nickel particle inserts, as they are randomly oriented inside the nickel nanocrystals, on their mechanical strength. Although fabricating such a configuration is practically very difficult, our simulations will show the efficiency of the system if graphene particles are randomly arranged inside the grains. Figure 8(a) presents the compressive stress-strain curves of atomistic models with two different average grain sizes, with and without randomly oriented nickel particles, under the fast loading condition along the z direction. It can be seen that almost no improvement in the strength of the nanocrystalline systems is evident. The compressive stress-strain curves of the same material system with the loading along x and y directions are also presented in Fig. S5 [45]. The role of graphene inserts in the deformation mechanism is shown in Figs. 8(b)–8(e) and S6 [45]. Similar to the graphene interlayers in the previous simulations, the graphene particles have successfully blocked some dislocations from propagating [Figs. 8(e) and S6(c), S6(e), and S6(f)]. However, some dislocations have initiated from the tip of the graphene inserts [Figs. 8(d) and S6(a)]. In nanocrystalline metals, since the grain sizes are too small, there is no enough space for dislocations to initiate and grow inside the grains [35]. Furthermore, the MD simulations start from a defect-free grains condition [35]. Therefore, dislocations tend to initiate at the regions where a discontinuity in the crystalline structure exists, i.e., from the grain boundaries or from the tip of the graphene inserts. When the graphene inserts are arranged in a layerwise order inside the nanocrystalline matrix, a dislocation initiated at the tip of a graphene nanosheet has a relatively high chance to be blocked by the graphene nanosheets placed in the next interlayer region. In contrast, the material system reinforced with randomly oriented graphene nanosheets does not optimally benefit from this capability. Therefore, the layerwise arrangement of the graphene particles inside the material system plays a key role in strengthening the material.

In the case of randomly oriented graphene reinforcements, the dislocation initiating and dislocation blocking contributions of the graphene particles have cancelled out one another's

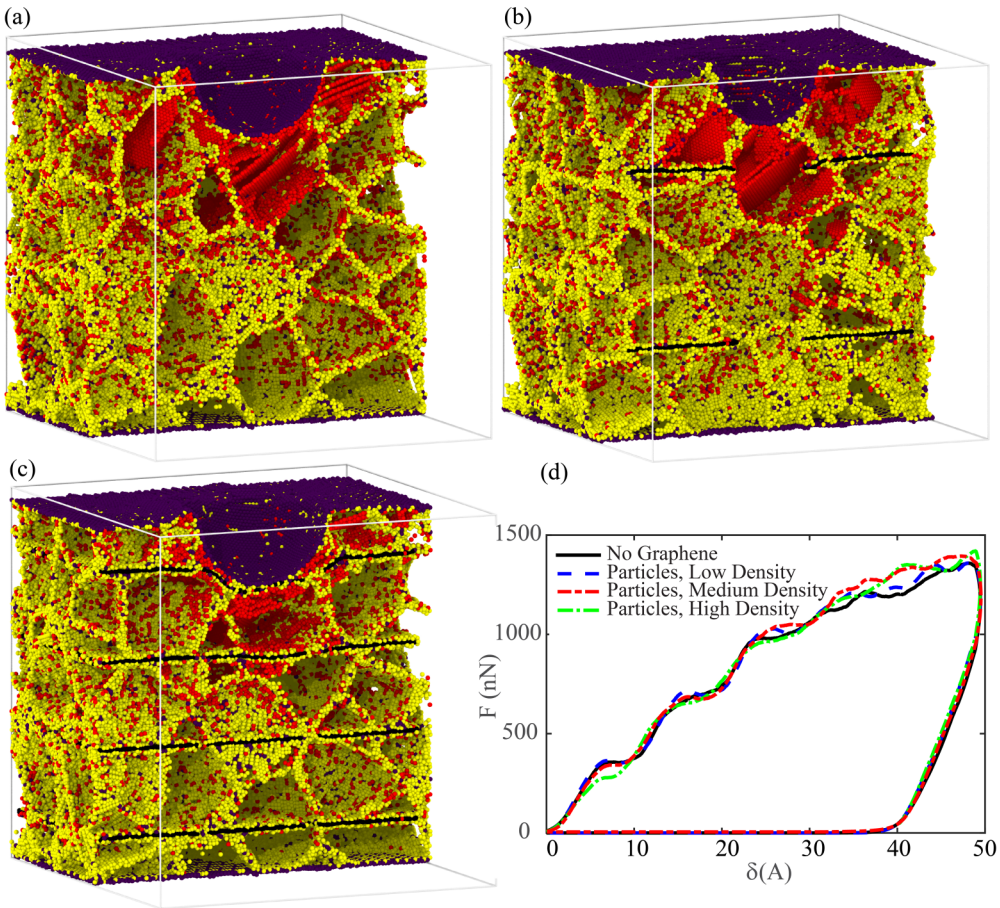

FIG. 9. Nickel nanocrystals reinforced with (a) no graphene and (b) low and (c) high areal coverage of graphene particles under indentation loadings. (d) Load-depth curves of the nanoindentation simulations showing that the simulations with medium and high densities of graphene interlayers, on average, require higher levels of indentation force at a certain penetration depth.

effect on the strength of the system, resulting in no significant change in the compressive stress-strain behavior.

5. Nanoindentation

In order to study the effects of reinforcing graphene interlayers under more complicated loading situations a series of atomistic models is developed to simulate the response of graphene reinforced systems to a nanoindentation loading. Comparing the simulations with real-life indentation loadings, the simulations loading rate is much higher. However, it is shown in the literature [27,50] that for the average grain size of 4.9 to 12.1 nm and indentation depth of around 2.7 nm the nanoindentation simulations are in a good qualitative agreement with experimental results. Therefore, satisfying these conditions, our paper is qualitatively valid.

Our simulated nanocrystalline nickel systems are only reinforced with graphene particles, not full sheets of graphene. However, various areal fractions of particles are introduced into the models, as low, medium, and high densities. The developed atomistic models, under indentation loadings, are shown in Figs. 9(a)–9(c). Figure 9(a), which is the system with no graphene particles, shows how a high density of dislocations is developed under the indenter head and propagated through the thickness of the polycrystal. Low density of graphene particles, in Fig. 9(b), however, has partially blocked the dislocations. In contrast, the model with high density of graphene particles in Fig. 9(c) shows the effect of graphene particles to block the attack of dislocations to the lower layers of nickel nanocrystal. This is the reason that in the load-depth curves of Fig. 9(d) the nickel-graphene systems with medium and high graphene particle contents shows higher required loads for indentation to a given depth.

B. Experimental results

As previously discussed, fabrication of nickel-graphene nanolayered composites inspired by the results of molecular-dynamics simulations is attempted. The fabricated composites possess various areal coverages of monolayer graphene particles at their interlayers. The composites undergo nanoindentation loadings to determine an optimum areal coverage of graphene particles able to strengthen the nanocrystalline nickels at a high level.

1. Graphene interlayers

The nickel films covered with different concentrations of graphene dispersions are studied under a field-emission scanning electron microscope, shown in Fig. 10, to examine their graphene coverage. As shown in Fig. 10, as graphene concentration increases, the areal coverage over the nickel layers increases. The FE-SEM micrographs, taken from different zones and with different magnifications, are analyzed using an image processing tool called ImageJ, to quantify the areal coverage of graphene particles in the interlayer regions. As the result, D, M, H, and SH sample configurations demonstrated 13.7 ± 0.59, 22.2 ± 1.00, 26.2 ± 1.89, and $34.3 \pm 0.44\%$ graphene areal coverage, respectively, in their interlayer regions. However, with increase in the graphene concentration, more agglomerated graphene flakes remain on the nickel surface. These agglomerates in the interlayer regions potentially provide unwanted discontinuity in the nanolayered composites structures which can limit the capability of the graphene layer in interlocking the dislocations growth inside the structure. However, when the nanolayered composites are under loading conditions and dislocations grow in a metal

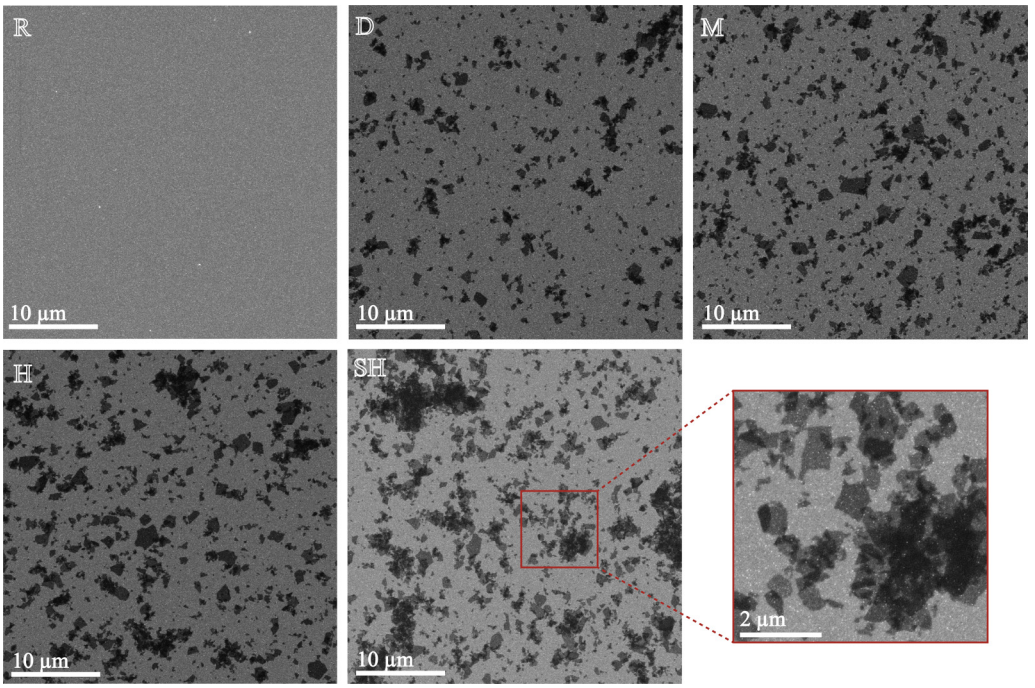

FIG. 10. The nickel films covered with different concentrations of graphene dispersion. D, M, H, and SH have undergone the spin coatings of graphene dispersion concentrations of 0.025, 0.050, 0.075, and 0.100 wt. %, respectively, and the R sample did not have any graphene layer. Graphene agglomerates can be observed as graphene content in the dispersion increases, as shown in the magnified picture.

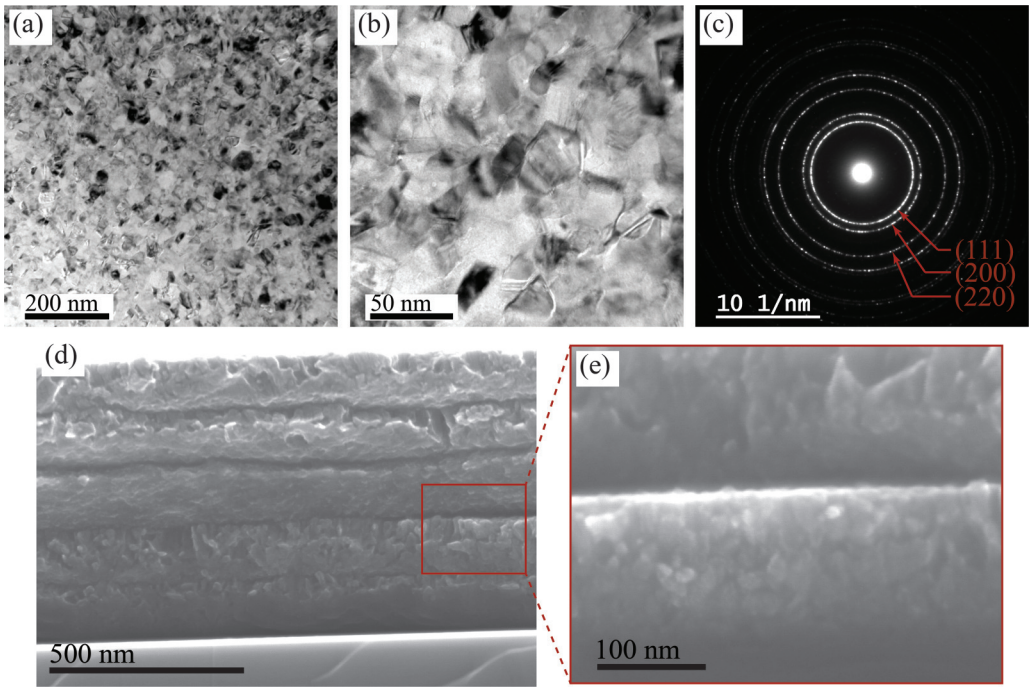

FIG. 11. TEM images of nickel thin layers shown at different magnifications in panels (a) and (b). The grain size is ranging from a few nanometers up to 40 nm with an average size of 18.3 nm. (c) SADPs revealing the nanocrystalline structure of the nickel layers corresponding to FCC nickel structure with no preferred crystal orientation. (d) and (e) Cross-sectional SEM images of the nickel nanolayered composites at two different magnifications.

layer, wider areal coverage of graphene flakes increases the desired chance of dislocations being stopped.

2. *Nickel layers*

The crystalline structure of the nanolayered nickel composites is shown in the micrographs of Fig. 11. Bright field TEM images of deposited nickel layers, shown in Figs. 11(a) and 11(b), confirms that the nickel layers possess a polycrystalline structure with grains diameters ranging from a few nanometers up to 40 nm. The average grain size of the nanocrystalline structure is measured to be 18.3 nm, which is close to the optimum grain size corresponding to the strongest nickel nanocrystalline structure (∼12 nm). The SADP, shown in Fig. 11(c), exhibited three complete shining rings revealing that the grown nanograins have no preferred crystal orientations. Circle Hough transform analysis of the SADP is performed to calculate the interplanar spacing (d spacing) associated with the distinct circles. It is revealed that the calculated interplanar lattice spacings correspond to the ones known for face-centered cubic (FCC) nickel.

The layered structure of the designed nanolayered composites is shown in the cross-sectional SEM image of Fig. 11(d). The magnified inset illustrates the crystalline structure from the side view. The nickel nanosized grains can be observed in this picture. The grain sizes detected in this SEM micrograph are similar to the ones in the TEM images of Fig. 11(a).

3. *Nanoindentation*

The representative load-depth curves of the load-controlled performed nanoindentation tests are plotted in Figs. 12(a)–12(c) for maximum indentation loads of 5.0, 10.0, and 20.0 mN, respectively. A strengthening effect of graphene particles at the interlayers can be seen for the nickel-graphene systems with low graphene content (dilute), for which at a given input load the nickel-graphene system has undergone less penetration depth. In contrast, the nickel-graphene systems with the highest graphene particle contents (superhigh) underwent deeper penetration. From the load-depth curves for all the individual indentations, average hardness and reduced moduli of the samples are obtained and shown in Figs. 12(d) and 12(e), respectively. For almost all the load cases, the nickel-graphene systems with dilute, medium, and high contents of graphene particle interlayers exhibit improvements in hardness. Particularly, 39% improvement in the hardness of nanocrystalline nickel is observed for the dilute sample at the maximum load of 10.0 mN. The capability of the graphene particle interlayers in blocking the dislocations inside the nickel grains, as observed in the numerical simulations, can be the main reason for the hardening effects observed in the experiments. However, for the superhigh content of graphene particles, an evident drop in hardness can be observed. This can be due to the existence of graphene agglomerates in the interlayer regions shown in Fig. 10. In summary, the high concentration of graphene particles in the solution used in fabricating this specific sample configuration is the reason behind decrement in hardness.

The reduced modulus is calculated using a curve fitting at the unloading part of the load-depth curves. Taking the standard deviation into account, no significant change was observed in the reduced modulus of the nickel-graphene nanolayered composites. Retaining the elastic modulus confirms that this method of integrating the graphene nanosheets has not changed the interatomic bonding in the nickel nanocrystalline structure [51].

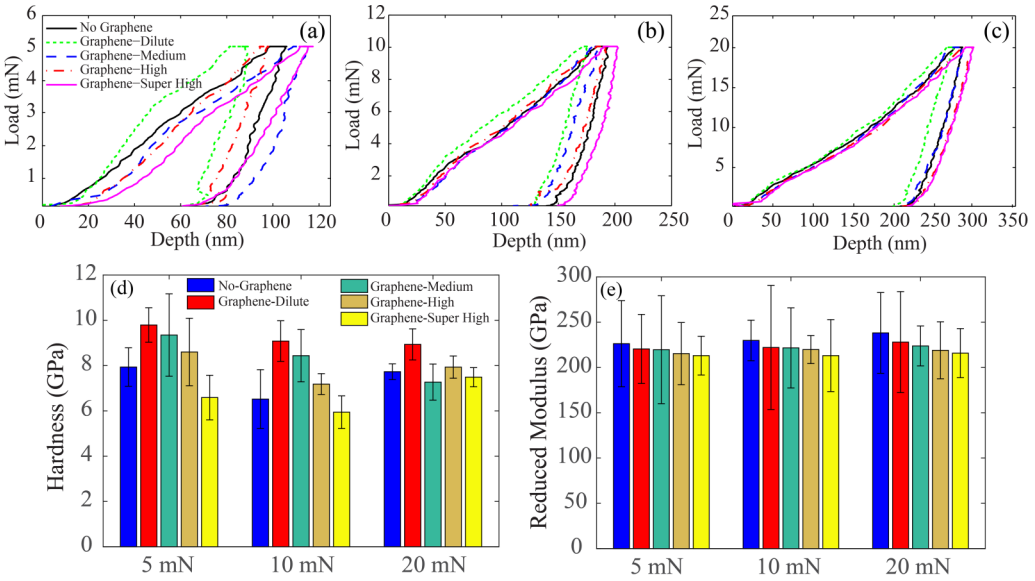

FIG. 12. The representative load-depth curves of the load-controlled performed nanoindentation tests for maximum indentation loads of (a) 5.0 mN, (b) 10.0 mN, and (c) 20.0 mN. (d and e) Average of the obtained results: (d) hardness and (e) reduced modulus. The nickel-graphene nanolayered composite with ∼13.7% areal coverage of graphene particles at the interlayers is the optimum configuration with the highest improvements in the hardness.

IV. CONCLUSIONS

In the present paper, we introduced a nickel-graphene nanolayered composite system in which instead of reinforcing large individual graphene sheets in the interlayer area monolayer graphene flakes are spread inside the interlayers. In this composite only a fraction of the interlayer area (13–30%) is covered. This graphene-metal nanolayered composite system is relatively easy and cost effective to fabricate in large scales. In the first steps of this paper, a systematic investigation of the effect of various graphene reinforcement configurations on a nickel-graphene system's performance is performed by utilizing a series of atomistic simulations. The molecular-dynamics simulations of various nanocrystalline nickel-graphene systems are performed for a polycrystalline system under both compression and nanoindentation loadings to reveal the effects of metal average grain size, simulation cell size, graphene reinforcements' configuration, and loading rate. It is revealed that at a certain average grain size range (∼12 nm) the nanocrystalline nickel illustrates a maximum strength. This is due to the fact that the plastic deformation mechanism transfers from a Hall-Petch regime, governed by dislocation growth inside the grains, into a reverse Hall-Petch regime, governed by atomic sliding at the grain boundaries. Our atomistic simulations were successfully able to capture this transfer in the deformation mechanisms. It is also revealed that graphene full sheets and particles can effectively hinder dislocations growth and atomic sliding, fully or partially, resulting in strengthening the material system under compression. However, when graphene particles were randomly oriented inside the polycrystalline nickel, no meaningful change in the strength was observed. Moreover, the molecular-dynamics simulations of nanoindentation loadings confirmed the role of graphene particle interlayers in hardening of material systems via hindering the dislocation growth through the metal grains. Inspired by the results of the atomistic simulations, the best applicable nickel-graphene nanolayered systems (with an average grain size of 18.3 nm, which is very close to the optimum grain size corresponding to the maximum strength of nickel polycrystals) are identified and fabricated. The fabricated nickel-graphene nanolayered composites are mechanically characterized with nanoindentation experiments to quantify their hardness. The experimental results show that a nickel-graphene nanolayered system, with only 14% areal coverage of graphene particles at the interlayer, has improved the hardness of the nanocrystalline nickel by almost 40%. As the result of this investigation, it is confirmed that the introduced material system benefits from both the nanocrystallinity of the metal as well as the strengthening effects of the graphene interlayers.

ACKNOWLEDGMENT

The authors acknowledge Advanced Research Computing at Virginia Tech (URL: http://www.arc.vt.edu) for providing computational resources and technical support that have contributed to the results reported within this paper.

F.Y. and A.Y.B. contributed equally to this paper.

[1] R. H. Baughman, A. A. Zakhidov, and W. A. De Heer, Carbon nanotubes: The route toward applications, Science **297**, 787 (2002).

[2] C. Lee, X. Wei, J. W. Kysar, and J. Hone, Measurement of the elastic properties and intrinsic strength of monolayer graphene, Science **321**, 385 (2008).

[3] A. K. Geim, Graphene: Status and prospects, Science **324**, 1530 (2009).
[4] R. Mirzaeifar, Z. Qin, and M. J. Buehler, Mesoscale mechanics of twisting carbon nanotube yarns, Nanoscale **7**, 5435 (2015).
[5] F. Yazdandoost, R. Mirzaeifar, Z. Qin, and M. J. Buehler, Multiscale mechanics of the lateral pressure effect on enhancing the load transfer between polymer coated CNTs, Nanoscale **9**, 5565 (2017).
[6] T. Kuzumaki, K. Miyazawa, H. Ichinose, and K. Ito, Processing of carbon nanotube reinforced aluminum composite, J. Mater. Res. **13**, 2445 (1998).
[7] S. I. Cha, K. T. Kim, S. N. Arshad, C. B. Mo, and S. H. Hong, Extraordinary strengthening effect of carbon nanotubes in metal-matrix nanocomposites processed by molecular-level mixing, Adv. Mater. **17**, 1377 (2005).
[8] K. T. Kim, S. I. Cha, T. Gemming, J. Eckert, and S. H. Hong, The role of interfacial oxygen atoms in the enhanced mechanical properties of carbon-nanotube-reinforced metal matrix nanocomposites, Small **4**, 1936 (2008).
[9] L. B. Johannes, L. L. Yowell, E. Sosa, S. Arepalli, and R. S. Mishra, Survivability of single-walled carbon nanotubes during friction stir processing, Nanotechnology **17**, 3081 (2006).
[10] Y. Morisada, H. Fujii, T. Nagaoka, and M. Fukusumi, MWCNTs/AZ31 surface composites fabricated by friction stir processing, Mater. Sci. Eng. A **419**, 344 (2006).
[11] G. Chai, Y. Sun, and Q. Chen, Mechanical properties of carbon nanotube-copper nanocomposites, J. Micromech. Microeng. **18**, 035013 (2008).
[12] S. F. Bartolucci, J. Paras, M. A. Rafiee, J. Rafiee, S. Lee, D. Kapoor, and N. Koratkar, Graphene-aluminum nanocomposites, Mater. Sci. Eng. A **528**, 7933 (2011).
[13] L. Jiang, G. Fan, Z. Li, X. Kai, D. Zhang, Z. Chen, S. Humphries, G. Heness, and W. Y. Yeung, An approach to the uniform dispersion of a high volume fraction of carbon nanotubes in aluminum powder, Carbon **49**, 1965 (2011).
[14] J. Wang, Z. Li, G. Fan, H. Pan, Z. Chen, and D. Zhang, Reinforcement with graphene nanosheets in aluminum matrix composites, Scr. Mater. **66**, 594 (2012).
[15] R. Pérez-Bustamante, D. Bolaños-Morales, J. Bonilla-Martínez, I. Estrada-Guel, and R. Martínez-Sánchez, Microstructural and hardness behavior of graphene-nanoplatelets/aluminum composites synthesized by mechanical alloying, J. Alloys Compd. **615**, S578 (2014).
[16] C.-H. Jeon, Y.-H. Jeong, J.-J. Seo, H. N. Tien, S.-T. Hong, Y.-J. Yum, S.-H. Hur, and K.-J. Lee, Material properties of graphene/aluminum metal matrix composites fabricated by friction stir processing, International Journal of Precision Engineering and Manufacturing **15**, 1235 (2014).
[17] T. S. Koltsova, L. I. Nasibulina, I. V. Anoshkin, V. V. Mishin, E. I. Kauppinen, O. V. Tolochko, and A. G. Nasibulin, New hybrid copper composite materials based on carbon nanostructures, J. Mater. Sci. Eng. B **2**, 240 (2012).
[18] J. Hwang, T. Yoon, S. H. Jin, J. Lee, T. S. Kim, S. H. Hong, and S. Jeon, Enhanced mechanical properties of graphene/copper nanocomposites using a molecular-level mixing process, Adv. Mater. **25**, 6724 (2013).
[19] C. L. Pavithra, B. V. Sarada, K. V. Rajulapati, T. N. Rao, and G. Sundararajan, A new electrochemical approach for the synthesis of copper-graphene nanocomposite foils with high hardness, Scientific Reports **4**, 4049 (2014).
[20] Y. Tang, X. Yang, R. Wang, and M. Li, Enhancement of the mechanical properties of graphene-copper composites with graphene-nickel hybrids, Mater. Sci. Eng. A **599**, 247 (2014).
[21] L.-Y. Chen, H. Konishi, A. Fehrenbacher, C. Ma, J.-Q. Xu, H. Choi, H.-F. Xu, F. E. Pfefferkorn, and X.-C. Li, Novel nanoprocessing route for bulk graphene nanoplatelets reinforced metal matrix nanocomposites, Scr. Mater. **67**, 29 (2012).
[22] D. Kuang, L. Xu, L. Liu, W. Hu, and Y. Wu, Graphene-nickel composites, Appl. Surf. Sci. **273**, 484 (2013).
[23] Y. Kim, J. Lee, M. S. Yeom, J. W. Shin, H. Kim, Y. Cui, J. W. Kysar, J. Hone, Y. Jung, S. Jeon, and S. M. Han, Strengthening effect of single-atomic-layer graphene in metal-graphene nanolayered composites, Nat. Commun. **4**, 2114 (2013).
[24] R. G. Hoagland, R. J. Kurtz, and C. H. Henager, Slip resistance of interfaces and the strength of metallic multilayer composites, Scr. Mater. **50**, 775 (2004).
[25] J. Wang, R. Hoagland, J. Hirth, and A. Misra, Atomistic simulations of the shear strength and sliding mechanisms of copper-niobium interfaces, Acta Materialia **56**, 3109 (2008).
[26] J. Wang, R. Hoagland, J. Hirth, and A. Misra, Atomistic modeling of the interaction of glide dislocations with "weak" interfaces, Acta Materialia **56**, 5685 (2008).
[27] S.-W. Chang, A. K. Nair, and M. J. Buehler, Nanoindentation study of size effects in nickel-graphene nanocomposites, Philos. Mag. Lett. **93**, 196 (2013).
[28] S. E. Muller and A. K. Nair, Dislocation nucleation in nickel-graphene nanocomposites under mode I loading, JOM **68**, 1909 (2016).
[29] E. Hall, The deformation and ageing of mild steel III: Discussion of results, Proc. Phys. Soc. London, Sect. B **64**, 747 (1951).
[30] N. Petch, The cleavage strength of polycrystals, J. Iron Steel Inst. **174**, 25 (1953).
[31] J. Schiøtz, F. D. Di Tolla, and K. W. Jacobsen, Softening of nanocrystalline metals at very small grain sizes, Nature (London) **391**, 561 (1998).
[32] J. Schiøtz, T. Vegge, F. D. Di Tolla, and K. W. Jacobsen, Atomic-scale simulations of the mechanical deformation of nanocrystalline metals, Phys. Rev. B **60**, 11971 (1999).
[33] H. Van Swygenhoven, M. Spaczer, A. Caro, and D. Farkas, Competing plastic deformation mechanisms in nanophase metals, Phys. Rev. B **60**, 22 (1999).
[34] H. Van Swygenhoven, A. Caro, and D. Farkas, A molecular dynamics study of polycrystalline fcc metals at the nanoscale: Grain boundary structure and its influence on plastic deformation, Mater. Sci. Eng. A **309**, 440 (2001).
[35] J. Schiøtz and K. W. Jacobsen, A maximum in the strength of nanocrystalline copper, Science **301**, 1357 (2003).
[36] D. Farkas and W. A. Curtin, Plastic deformation mechanisms in nanocrystalline columnar grain structures, Mater. Sci. Eng. A **412**, 316 (2005).
[37] J. Uddin, M. I. Baskes, S. G. Srinivasan, T. R. Cundari, and A. K. Wilson, Modified embedded atom method study of the mechanical properties of carbon nanotube reinforced nickel composites, Phys. Rev. B **81**, 104103 (2010).
[38] S. Plimpton, Fast parallel algorithms for short-range molecular dynamics, J. Comput. Phys. **117**, 1 (1995).
[39] A. Stukowski, Visualization and analysis of atomistic simulation data with OVITO: The Open Visualization Tool, Modell. Simul. Mater. Sci. Eng. **18**, 015012 (2009).

[40] B. N. Boots, The arrangement of cells in random networks, Metallography **15**, 53 (1982).
[41] J. Matthews, *Epitaxial Growth* (Elsevier, New York, 2012).
[42] R. Mirzaeifar, K. Gall, T. Zhu, A. Yavari, and R. DesRoches, Structural transformations in NiTi shape memory alloy nanowires, J. Appl. Phys. **115**, 194307 (2014).
[43] F. Yazdandoost and R. Mirzaeifar, Tilt grain boundaries energy and structure in NiTi alloys, Comput. Mater. Sci. **131**, 108 (2017).
[44] F. Yazdandoost and R. Mirzaeifar, Generalized stacking fault energy and dislocation properties in NiTi shape memory alloys, J. Alloys Compd. **709**, 72 (2017).
[45] See Supplemental Material at http://link.aps.org/supplemental/10.1103/PhysRevMaterials.1.076001 for more studies under various loading modes.
[46] W. C. Oliver and G. M. Pharr, An improved technique for determining hardness and elastic modulus using load and displacement sensing indentation experiments, J. Mater. Res. **7**, 1564 (1992).
[47] W. C. Oliver and G. M. Pharr, Measurement of hardness and elastic modulus by instrumented indentation: Advances in understanding and refinements to methodology, J. Mater. Res. **19**, 3 (2004).
[48] A. Lund and C. Schuh, Strength asymmetry in nanocrystalline metals under multiaxial loading, Acta Materialia **53**, 3193 (2005).
[49] K. Zhou, B. Liu, S. Shao, and Y. Yao, Molecular dynamics simulations of tension-compression asymmetry in nanocrystalline copper, Phys. Lett. A **381**, 1163 (2017).
[50] D. Mordehai, M. Kazakevich, D. J. Srolovitz, and E. Rabkin, Nanoindentation size effect in single-crystal nanoparticles and thin films: A comparative experimental and simulation study, Acta Materialia **59**, 2309 (2011).
[51] S. Hao, L. Cui, D. Jiang, X. Han, Y. Ren, J. Jiang, Y. Liu, Z. Liu, S. Mao, and Y. Wang, A transforming metal nanocomposite with large elastic strain, low modulus, and high strength, Science **339**, 1191 (2013).